nature geoscience

ARTICLES
https://doi.org/10.1038/s41561-018-0160-2

Episodic creep events on the San Andreas Fault caused by pore pressure variations

Mostafa Khoshmanesh* and Manoochehr Shirzaei

Recent seismic and geodetic observations indicate that interseismic creep rate varies in both time and space. The spatial extent of creep pinpoints locked asperities, while its temporary accelerations, known as slow-slip events, may trigger earthquakes. Although the conditions promoting fault creep are well-studied, the mechanisms for initiating episodic slow-slip events are enigmatic. Here we investigate surface deformation measured by radar interferometry along the central San Andreas Fault between 2003 and 2010 to constrain the temporal evolution of creep. We show that slow-slip events are ensembles of localized creep bursts that aseismically rupture isolated fault compartments. Using a rate-and-state friction model, we show that effective normal stress is temporally variable on the fault, and support this using seismic observations. We propose that compaction-driven elevated pore fluid pressure in the hydraulically isolated fault zone and subsequent frictional dilation cause the observed slow-slip episodes. We further suggest that the 2004 M_w 6 Parkfield earthquake might have been triggered by a slow-slip event, which increased the Coulomb failure stress by up to 0.45 bar per year. This implies that while creeping segments are suggested to act as seismic rupture barriers, slow-slip events on these zones might promote seismicity on adjacent locked segments.

Fault creep, which accounts for the release of up to half of the seismic moment budget, is a pivotal component of the earthquake cycle[1]. The spatial extent of creep and its rate determine the degree to which a fault is locked and frequency of earthquakes[2,3]. Creeping behaviour is mainly attributed to geometrical complexity[4] and frictional strength of the fault zone material, with the latter in turn depending on lithology[5–7], temperature[8] and pore fluid pressure[9,10]. Temporary episodes of creep acceleration, known as slow-slip events (SSEs), have been interpreted as earthquake precursors and as a possible triggering factor for major earthquakes[11–15]. Ambient stress perturbations due to nearby earthquakes[16–18] and transient pore fluid pressure changes[9] are among the major causes of these creep events. However, recent observations indicate that SSEs can occur semi-periodically in different tectonic settings[13,19,20], which places additional constraints on the underlying mechanism. In this study, we provide evidence for episodic SSEs on a creeping transform boundary fault and their interaction with seismicity on surrounding locked segments, and suggest a physically plausible mechanism explaining the occurrence of these events.

SSE on the central San Andreas Fault

The 130 km central segment of the San Andreas Fault (CSAF) in California is characterized by a fast creep of rate $\sim$3 cm yr^{-1}, and is surrounded by two major locked segments that were the sources of the moment magnitude (M_w) 7.9 earthquakes of 1857 and 1906. The continuous creep on the CSAF is attributed to the frictional weakness, suggested by the lack of elevated heat flow[21] and nearly fault-normal orientation of maximum horizontal stress[22]. The frictional weakness, likely caused by intrinsic low friction of fault zone material[5–7] and abnormally elevated pore pressure within the fault core[9,23], suggests that the CSAF is incapable of storing enough strain to generate large earthquakes. Yet, episodic unsteady slip with limited speed in the form of SSEs are observed over the entire seismogenic depth of the CSAF at semi-regular intervals[19,20], which might modulate the time of seismic events on nearby locked zones. Although the maximum rate of these SSEs does not exceed several times the plate boundary shear strain rate, they share all other characteristics of the well-known SSEs on the subduction zones[19,20]. Stress transfer from nearby seismic events[16–18], transient inflow of fluid from depth into seismogenic zone[9] and shallow frictional heterogeneity[24] are suggested to trigger SSEs on the CSAF and nearby creeping segments. Availability of dense geodetic and seismic measurements and observations of the CSAF fault properties at the San Andreas Fault Observatory at Depth (SAFOD)[5,6] provide the opportunity to investigate the mechanism that drives SSEs and controls their velocity, duration and repeat time.

We used the time series of line-of-sight (LOS) surface deformation obtained from interferometric processing of the synthetic aperture radar (SAR) dataset, collected between 26 March 2003 and 7 July 2010 with an average temporal sampling interval of approximately two months, to measure surface fault creep (Fig. 1 and Supplementary Movie 1). The dataset was obtained[20,25] by applying an advanced multitemporal interferometric SAR (InSAR) processing algorithm[26] on 16 and 30 images acquired by the European Remote Sensing (ERS) and Envisat C-band satellites, respectively. These LOS observations are thoroughly validated in refs [20,25] using independent geodetic observations (see also Supplementary Fig. 1). Here we calculate the near-field LOS creep time series[27] using a moving window of 0.5 km × 2.7 km (from 0.3 to 3 km fault-normal distance) and along-strike step size of 0.3 km (inset in Fig. 1). The observations of near-field LOS creep reflect the slip behaviour of the shallow few kilometre portion of the fault, which might have a similar pattern to that of deeper seismogenic depths[20,28]. The spatiotemporal distribution of the difference between short- and long-term LOS creep rate along the CSAF depicts the local variations of creep rate in both space and time (Fig. 2). To increase the signal to noise ratio, we averaged the rate differences in the spatial domain (magenta curve in Fig. 3a and Supplementary Fig. 2), which reveals the semi-periodic SSEs. To focus on the interseismic slip and disregarding the co- and post-seismic deformations due

School of Earth and Space Exploration, Arizona State University, Tempe, AZ, USA. *e-mail: mkhm@asu.edu

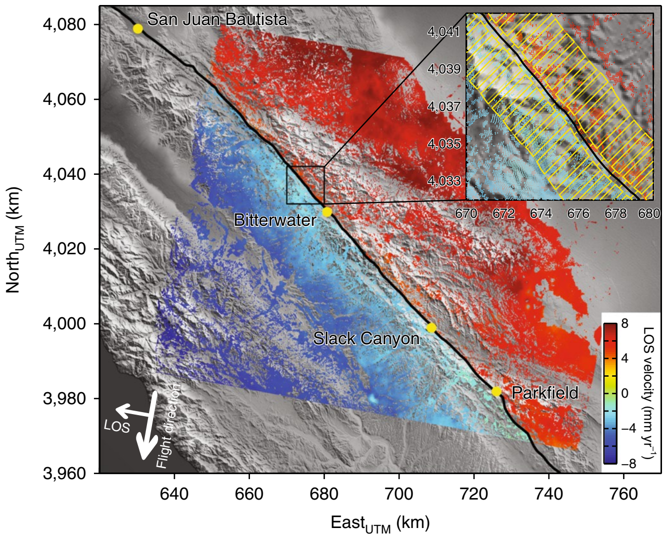

Fig. 1 | Creeping segment of the San Andreas Fault with long-term InSAR LOS velocity[20,25]. The trace of the SAF is shown with the black line. Warm and cold colours correspond, respectively, to the movement towards and away from the descending satellite. The inset depicts the moving window (yellow boxes) used for estimation of near-field creep rate, with every other step shown with a lower opacity for visualization purposes. Shaded relief topography is the digital elevation model from the Shuttle Radar Topography Mission. UTM, Universal Transverse Mercator coordinate system.

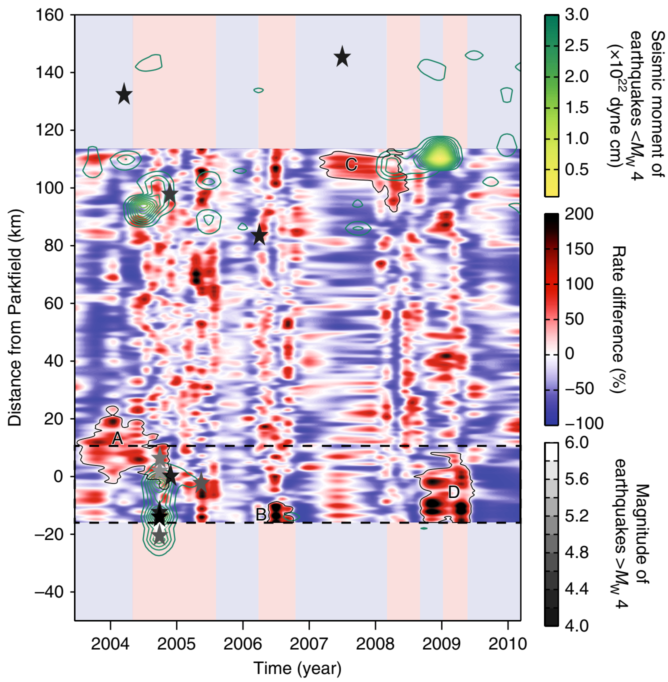

Fig. 2 | Spatiotemporal distribution of rate difference and seismicity. The relative difference between short-term (between consecutive time steps) and long-term LOS creep rate (slope of the cumulative time series) in percentage, along with moment released for earthquakes <M_w 4 (green contours). Greyscale stars show the location and time of the earthquakes >M_w 4. The light red and blue bands on the neighbouring segments highlight the time intervals of SSEs and the decelerated creeping, respectively. The dashed rectangle shows the approximate location of the Parkfield transition zone, which is excluded from our analyses. The areas indicated by capital letters show the extent of the significant local bursts that are discussed in the main text.

to the 2004 Parkfield earthquake in our analysis, we exclude the affected observations (inside the black dashed rectangle in Fig. 2). Then, the roughness of LOS creep distribution along the fault is estimated through self-affinity analysis[29] implemented on the fault-parallel profiles of rate difference at each time step (see Methods). The roughness amplitude also exhibits time-dependent behaviour (black curve in Fig. 3b), which has an 87 ± 3% correlation with creep rate difference. This means that surface LOS creep is rougher during SSEs, likely due to more heterogeneous creep distribution on the fault. In other words, each observed SSE results from an ensemble of localized creep bursts, namely clusters of accelerated creep exceeding the long-term rate[27]. These bursts aseismically rupture isolated fault segments, separated by stable creeping patches, instead of a single burst rupturing the entire extent of the fault.

Possible mechanisms of SSEs

To nucleate SSEs, several mechanisms are suggested, including velocity-weakening frictional properties of certain materials at very low velocities[30,31] and frictional strength reduction with steady slip, that is, slip weakening[32]. Stress perturbations due to nearby earthquakes or pore pressure variations are also suggested to generate transient SSEs on the unstable–stable transition zone with velocity-neutral properties[33]. In contrast, switching to velocity-strengthening properties at higher (subseismic) creep rates[30,31] and frictional dilation leading to a reduction of pore pressure[34] are proposed as mechanisms for arresting the premature slip in SSEs, preventing these events from turning into an earthquake. The combination of these nucleation and arrest mechanisms are used to simulate SSEs on the downdip end of the seismogenic zone in subduction faults[33], where creep velocity reaches up to 10^2–10^3 times the tectonic shearing rate[11,35]. However, much slower semi-periodic accelerated creep events that are shown to occur on the entire seismogenic depth of the CSAF[19,20], which exhibits velocity-strengthening properties[5,6], likely belong to a new class of SSEs. These require a new explanation perhaps based on localized perturbation of shear strength on the fault[36].

The common aspect of the aforementioned mechanisms for initiation of SSEs is the requirement of a constant or transient near-lithostatic pore pressure. In subduction zones, elevated pore pressure is speculated to be caused by dehydration of hydrous minerals in a downgoing plate[10]. But, the mechanism for pore pressure fluctuations on crustal transform faults is less clear. The inflow of mantle-driven fluid[9,23] into the highly permeable active fault zone of the CSAF, as an existing hypothesis, implies a time lag between SSEs at different depths, which is not supported by slip models[20]. Thermal pressurization due to shear heating[37] is an alternative explanation for the elevation of pore pressure, which results in seismic rupture nucleation. However, this mechanism is significant only when creep rate reaches to orders of magnitude higher than the maximum rate of SSEs on the CSAF[37]. Compaction of intergranular pore spaces within the hydraulically isolated fault core[38–40], however, can serve as a viable mechanism for cyclic elevation of pore pressure on the CSAF. Elevated pore pressure in this mechanism is self-generating[40], and does not require an external fluid source.

Rate-and-state friction modelling

To investigate the role of pore pressure variation in generating SSEs, we quantify the time series of effective normal stress rate on the fault using a rate-and-state friction model under a steady-state condition (see Methods). The effective normal stress ($\sigma_e = \sigma_n - p$) is related to steady-state shear stress (τ_{ss}, Supplementary Fig. 3) through $\tau_{ss} = \sigma_e \left(f_0 + (a-b)\log\frac{V_{ss}}{V_0} \right)$, where σ_n is the tectonic normal stress and p is the pore pressure, f_0 is nominal coefficient of friction,

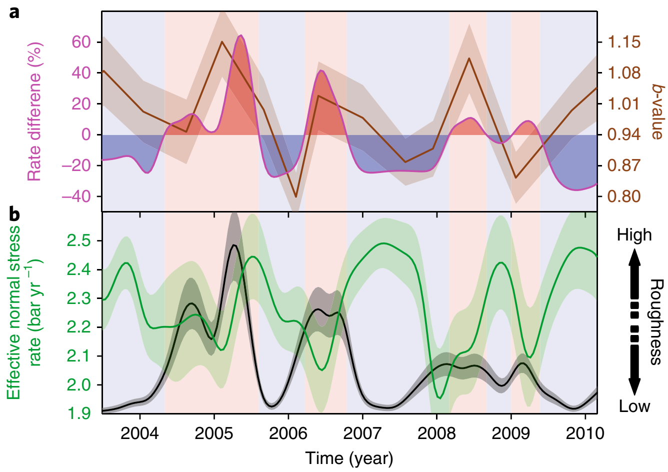

Fig. 3 | Temporal evolution of creep rate, effective normal stressing rate, roughness and *b*-value. a, Time series of spatially averaged LOS creep rate difference in percentage (magenta) and *b*-value (brown) alongside its one-sigma uncertainty (shaded brown). Background red and blue bands highlight the time interval of SSEs and decelerated creeping, respectively. **b**, Temporal evolution of spatially averaged effective normal stress rate (green) and its standard deviation (shaded green), and roughness amplitude of LOS creep rate difference along the fault (black) and its one-sigma uncertainty (shaded grey). All the curves in this figure, except the *b*-value, are smoothed using a Gaussian smoothing filter with a window size of six months.

$a-b$ is the frictional rate parameter, V_{ss} is the steady-state rate and V_0 is the reference creep rate[41]. The estimated effective normal stress rate (Supplementary Fig. 4) depicts the spatiotemporal variation of pore pressure along the CSAF, given that there is no evidence for a variable tectonic normal stressing rate during our study period. Averaging along the fault and comparing the temporal evolution of effective normal stress rate (green curve in Fig. 3b) with that of surficial creep rate difference, we find that an increase (decrease) in average LOS creep rate corresponds to a reduction (increase) in the effective normal stressing rate that we attribute to pore pressure elevation (reduction).

Insights from seismicity

Microseismicity, a distinguishing attribute of creeping faults[42], can also provide insight into the temporal evolution of fault strength and shed light on the possible mechanism for transient events. The temporal evolution of the estimated Gutenberg–Richter *b*-value[43] (Supplementary Figs. 5–7, brown curve in Fig. 3a, see Methods) exhibits a 60 ± 8% correlation with the variation of LOS creep rate difference, showing a clear increase in the *b*-value during the dominant SSEs on the CSAF. However, the reason for poor correlation starting in 2009 and before mid-2004 is unclear. Moreover, time series of the total seismic moment of microearthquakes exhibits a negative correlation with the *b*-value and surface creep rate (Supplementary Fig. 7). This suggests that larger microearthquakes (lower *b*-value) occur when the fault is creeping with a relatively slower rate[43], due to pore pressure drop leading to restrengthening of the fault. A similar conclusion can also be reached by comparing earthquake counts and the creep rate difference (Supplementary Fig. 8), which suggest that microseismic activity maximizes when the frictional strength is increased. This is followed by a decline in microseismicity when the pore pressure is elevated while the CSAF is experiencing an episode of slow-slip. Spatiotemporal distribution of seismic moment along the CSAF and adjacent locked segments is also overlain on the distribution of LOS creep rate difference (Supplementary Fig. 9). Comparisons confirm that segments with elevated seismic moment release are predominantly creeping slower than the long-term rate (indicated by the colder colours).

Preferred mechanism driving creep events on the SAF

Our observations and analyses suggest that elevated pore pressure possibly driven by compaction[38–40] and subsequent frictional dilation[34] are responsible for initiating and arresting the episodic SSEs along the CSAF. Within a dilated fault zone with an average pore pressure below lithostatic, intergranular pore spaces undergo compaction due to ductile creep[39]. Under an undrained condition, namely being hydraulically isolated from the surrounding country rock through a permanent impermeable seal layer[44], compaction results in increased pore pressure to lithostatic level[38,39], which correlates with incipient creep acceleration[45]. Considering a compressibility of 10^{-10} to $10^{-9}\,\mathrm{Pa}^{-1}$, a porosity reduction of 1–6% at depth of 8 km results in elevation of pore pressure from hydrostatic to lithostatic level. Due to the heterogeneous fault zone material and geometrical irregularity of the fault surface, however, rate of porosity reduction due to compaction is not the same for the entire fault, leading to heterogeneous distribution of overpressurized fluid on the fault[46,47]. Moreover, extremely low permeability of fault gouge on the CSAF (10^{-23} to $10^{-21}\,\mathrm{m}^2$)[48] reduces the rate of specific discharge from zones of elevated pore pressure. This divides the fault into natural compartments with different fluid pressures, resulting in a heterogeneous distribution of pore pressure across the seismogenic zone[40,49]. The isolated creep bursts, therefore, pinpoint the location of these overpressurized compartments along the CSAF. An ensemble of these localized creep bursts, observed as heterogeneous creep rates on the surface, which is quantified using increased roughness estimates, makes up the episodic SSEs.

In contrast, frictional dilation[34] due to accelerated creep restores the porosity and restrengthens the overpressurized compartments, which is correlated with the incipient creep deceleration[45]. Frictional dilation also increases the permeability of fault gouge, which leads to redistribution of fluid within the fault zone, and therefore homogenous distribution of pore pressure along the fault[38,39]. This coincides with decelerated creep rate with a spatially uniform pattern throughout the fault, observed as a smoother surface creep rate distribution (Supplementary Fig. 10), which also marks the initiation of the next compaction cycle. The increased effective normal stress during creep deceleration, causing negative Coulomb stress changes, may additionally trigger slip transients, which are characterized by significantly smaller amplitude, and temporal delays proportional to the size of stress perturbations[36]. Nonetheless, modulation of these dilation-induced slip transients onto the compaction-induced SSEs might be responsible for some of the irregularity that we observe in amplitude and timing of the SSEs on the CSAF.

In this mechanism, therefore, creep rate variation is not instantaneous, and instead, creep evolves in consecutive intervals of acceleration and deceleration, which correlate with similar variations in pore pressure. This is consistent with the results of laboratory experiments documenting the role of elevated pore pressure and decreased permeability in generating the transient events[45]. The observed concurrence of the decreased *b*-value and increased number of microseismic events and their released moment during the decelerated creep, when the frictional strength is elevated, is also aligned with our proposed mechanism for SSEs on the CSAF[38,40,49]. Our suggested mechanism does not require an external fluid source[38–40], which makes it a favourable explanation for the observed variation of creep rate on other velocity-strengthening crustal faults[28] and possibly subduction zones.

SSEs impact on seismic hazard

SSEs are suggested as a mechanism for triggering major earthquakes on subduction zones[11–13] and as also being triggered due to adjacent earthquakes on crustal faults[16–18]. Distribution of the seismicity[50] along the CSAF and the transition segment to the south (from −50 to 115 km in Fig. 2) reveal that earthquakes larger than M_w 4, including the 2004 M_w 6 Parkfield earthquake, occurred during SSEs on the CSAF. The timing of the earthquakes in the northern locked segment (from 115 to 160 km in Fig. 2), however, is not correlated with the timing of SSEs on the CSAF, perhaps due to more complex fault structure in this segment. Our observations show that initiation of the accelerated creep phase on the creeping segment precedes the 2004 earthquake, suggesting that this seismic event could have been triggered due to stress transfer from this SSE. We estimate that the rate of Coulomb stress change at the hypocentre (see Methods) increased up to 0.45 bar yr^{-1} during the SSE. In addition, the study of deep tremors suggested an SSE, possibly ~16 km below the hypocentre, preceded the Parkfield earthquake[14]. However, our geodetic observation does not provide adequate resolution to resolve the signal associated with this deep SSE.

Moreover, the ruptured asperity of the 2004 event slowly re-ruptured in the form of a localized burst during the following episodes of SSE on the CSAF (bursts B and D in Fig. 2). This calls for an additional explanation for the complex response of the Parkfield transition zone to the SSE on the CSAF, and most importantly the underlying triggering mechanism of the 2004 event. A closer examination of the creep rate difference distribution suggests that a combination of a significant localized burst (burst A in Fig. 2) initiated about one year before this event, persistent until the time of nucleation, and the SSE on the CSAF might have triggered this earthquake. Coseismic slip distribution of this earthquake[51] also suggests that the area experiencing the maximum coseismic slip has an overlap with the burst A. This is likely due to thermal pressurization of fluids[37] in addition to the pre-existing compaction-induced elevated pore pressure. This observation is also supported by a distinguishable increase in the microseismicity, following another significant local burst that occurred between 2007 to 2009 at the northern end of our study area (burst C in Fig. 2), with similar scale and amplitude to that of burst A. These findings highlight the role of observation and analyses of the surface creep rate to detect the SSEs and significant local bursts to improve the time-dependent estimates of seismic hazard associated with transform faults[27]. Moreover, considering the periodicity of these SSEs, as opposed to the conventional assumption of a constant loading rate, time-dependent probabilistic earthquake forecast models can be greatly improved.

Methods

Methods, including statements of data availability and any associated accession codes and references, are available at https://doi.org/10.1038/s41561-018-0160-2.

Received: 2 March 2018; Accepted: 18 May 2018;
[redacted]

References

1. Pacheco, J. F., Sykes, L. R. & Scholz, C. H. Nature of seismic coupling along simple plate boundaries of the subduction type. *J. Geophys. Res.* **98**, 14133–14159 (1993).
2. Perfettini, H. et al. Seismic and aseismic slip on the central Peru megathrust. *Nature* **465**, 78–81 (2010).
3. Chlieh, M. et al. Distribution of discrete seismic asperities and aseismic slip along the Ecuadorian megathrust. *Earth Planet. Sci. Lett.* **400**, 292–301 (2014).
4. Gao, X. & Wang, K. L. Strength of stick-slip and creeping subduction megathrusts from heat flow observations. *Science* **345**, 1038–1041 (2014).
5. Carpenter, B. M., Saffer, D. M. & Marone, C. Frictional properties of the active San Andreas Fault at SAFOD: implications for fault strength and slip behavior. *J. Geophys. Res.* **120**, 5273–5289 (2015).
6. Carpenter, B. M., Marone, C. & Saffer, D. M. Weakness of the San Andreas Fault revealed by samples from the active fault zone. *Nat. Geosci.* **4**, 251–254 (2011).
7. Lockner, D. A., Morrow, C., Moore, D. & Hickman, S. Low strength of deep San Andreas Fault gouge from SAFOD core. *Nature* **472**, 82–85 (2011).
8. Sibson, R. H. Fault zone models, heat flow, and the depth distribution of earthquakes in the continental crust of the United States. *Bull. Seismol. Soc. Am.* **72**, 151–163 (1982).
9. Rice, J. R. in *Earthquake Mechanics, Rock Deformation, and Transport Properties of Rocks* (eds Evans, B. & Wong, T.-F.) 475–503 (Academic Press, San Diego, 1992).
10. Kodaira, S. et al. High pore fluid pressure may cause silent slip in the Nankai Trough. *Science* **304**, 1295–1298 (2004).
11. Kato, A. et al. Propagation of slow slip leading up to the 2011 M_w 9.0 Tohoku-Oki earthquake. *Science* **335**, 705–708 (2012).
12. Schurr, B. et al. Gradual unlocking of plate boundary controlled initiation of the 2014 Iquique earthquake. *Nature* **512**, 299–302 (2014).
13. Uchida, N., Iinuma, T., Nadeau, R. M., Burgmann, R. & Hino, R. Periodic slow slip triggers megathrust zone earthquakes in northeastern Japan. *Science* **351**, 488–492 (2016).
14. Shelly, D. R. Possible deep fault slip preceding the 2004 Parkfield earthquake, inferred from detailed observations of tectonic tremor. *Geophys. Res. Lett.* **36**, L17318 (2009).
15. Radiguet, M. et al. Triggering of the 2014 M_w7.3 Papanoa earthquake by a slow slip event in Guerrero, Mexico. *Nat. Geosci.* **9**, 829–833 (2016).
16. Shelly, D. R., Peng, Z. G., Hill, D. P. & Aiken, C. Triggered creep as a possible mechanism for delayed dynamic triggering of tremor and earthquakes. *Nat. Geosci.* **4**, 384–388 (2011).
17. Wei, M., Liu, Y. J., Kaneko, Y., McGuire, J. J. & Bilham, R. Dynamic triggering of creep events in the Salton Trough, Southern California by regional $M = 5.4$ earthquakes constrained by geodetic observations and numerical simulations. *Earth Planet. Sci. Lett.* **427**, 1–10 (2015).
18. Shirzaei, M., Bürgmann, R. & Taira, T. A. Implications of recent asperity failures and aseismic creep for time-dependent earthquake hazard on the Hayward fault. *Earth Planet. Sci. Lett.* **371–372**, 59–66 (2013).
19. Nadeau, R. M. & McEvilly, T. V. Periodic pulsing of characteristic microearthquakes on the San Andreas Fault. *Science* **303**, 220–222 (2004).
20. Khoshmanesh, M., Shirzaei, M. & Nadeau, R. M. Time-dependent model of aseismic slip on the central San Andreas Fault from InSAR time series and repeating earthquakes. *J. Geophys. Res.* **120**, 6658–6679 (2015).
21. Williams, C. F., Grubb, F. V. & Galanis, S. P. Jr. Heat flow in the SAFOD pilot hole and implications for the strength of the San Andreas Fault. *Geophys. Res. Lett.* **31**, L15S14 (2004).
22. Zoback, M. D. et al. New evidence on the state of stress on the San Andreas Fault system. *Science* **238**, 1105–1111 (1987).
23. Fulton, P. M. & Saffer, D. M. Potential role of mantle-derived fluids in weakening the San Andreas Fault. *J. Geophys. Res.* **114**, B07408 (2009).
24. Wei, M., Kaneko, Y., Liu, Y. & McGuire, J. J. Episodic fault creep events in California controlled by shallow frictional heterogeneity. *Nat. Geosci.* **6**, 566–570 (2013).
25. Turner, R. C., Shirzaei, M., Nadeau, R. M. & Buergmann, R. Slow and go: pulsing slip rates on the creeping section of the San Andreas Fault. *J. Geophys. Res.* **120**, 5940–5951 (2015).
26. Shirzaei, M. A wavelet-based multitemporal DInSAR algorithm for monitoring ground surface motion. *IEEE Geosci. Remote Sens. Lett.* **10**, 456–460 (2013).
27. Khoshmanesh, M. & Shirzaei, M. Multiscale dynamics of aseismic slip on central San Andreas Fault. *Geophys. Res. Lett.* **45**, 2274–2282 (2018).
28. Jolivet, R. et al. The burst-like behavior of aseismic slip on a rough fault: the creeping section of the Haiyuan Fault, China. *Bull. Seismol. Soc. Am.* **105**, 480–488 (2015).
29. Schmittbuhl, J., Schmitt, F. & Scholz, C. Scaling invariance of crack surfaces. *J. Geophys. Res.* **100**, 5953–5973 (1995).
30. Shibazaki, B. & Lio, Y. On the physical mechanism of silent slip events along the deeper part of the seismogenic zone. *Geophys. Res. Lett.* **30**, 1489 (2003).
31. Kaproth, B. M. & Marone, C. Slow earthquakes, preseismic velocity changes, and the origin of slow frictional stick-slip. *Science* **341**, 1229–1232 (2013).
32. Ikari, M. J., Marone, C., Saffer, D. M. & Kopf, A. J. Slip weakening as a mechanism for slow earthquakes. *Nat. Geosci.* **6**, 468–472 (2013).
33. Liu, Y. J. & Rice, J. R. Spontaneous and triggered aseismic deformation transients in a subduction fault model. *J. Geophys. Res.* **112**, B09404 (2007).
34. Segall, P., Rubin, A. M., Bradley, A. M. & Rice, J. R. Dilatant strengthening as a mechanism for slow slip events. *J. Geophys. Res.* **115**, B12305 (2010).
35. Iio, Y., Kobayashi, Y. & Tada, T. Large earthquakes initiate by the acceleration of slips on the downward extensions of seismogenic faults. *Earth Planet. Sci. Lett.* **202**, 337–343 (2002).
36. Perfettini, H. & Ampuero, J. P. Dynamics of a velocity strengthening fault region: implications for slow earthquakes and postseismic slip. *J. Geophys. Res.* **113**, B09411 (2008).
37. Schmitt, S. V., Segall, P. & Matsuzawa, T. Shear heating-induced thermal pressurization during earthquake nucleation. *J. Geophys. Res.* **116**, B06308 (2011).
38. Sleep, N. H. & Blanpied, M. L. Creep, compaction and the weak rheology of major faults. *Nature* **359**, 687–692 (1992).

39. Sleep, N. H. Ductile creep, compaction, and rate and state dependent friction within major fault zones. *J. Geophys. Res.* **100**, 13065–13080 (1995).
40. Byerlee, J. Model for episodic flow of high-pressure water in fault zones before earthquakes. *Geology* **21**, 303–306 (1993).
41. Ruina, A. Slip instability and state variable friction laws. *J. Geophys. Res.* **88**, 10359–10370 (1983).
42. Malservisi, R., Furlong, K. P. & Gans, C. R. Microseismicity and creeping faults: hints from modeling the Hayward Fault, California (USA). *Earth Planet. Sci. Lett.* **234**, 421–435 (2005).
43. Tormann, T., Wiemer, S., Metzger, S., Michael, A. & Hardebeck, J. L. Size distribution of Parkfield's microearthquakes reflects changes in surface creep rate. *Geophys. J. Int.* **193**, 1474–1478 (2013).
44. Blanpied, M. L., Lockner, D. A. & Byerlee, J. D. An earthquake mechanism based on rapid sealing of faults. *Nature* **358**, 574–576 (1992).
45. Leclere, H., Faulkner, D., Wheeler, J. & Mariani, E. Permeability control on transient slip weakening during gypsum dehydration: implications for earthquakes in subduction zones. *Earth Planet. Sci. Lett.* **442**, 1–12 (2016).
46. Hillers, G. & Miller, S. A. Dilatancy controlled spatiotemporal slip evolution of a sealed fault with spatial variations of the pore pressure. *Geophys. J. Int.* **168**, 431–445 (2007).
47. Mittempergher, S. et al. Evidence of transient increases of fluid pressure in SAFOD phase III cores. *Geophys. Res. Lett.* **38**, L03301 (2011).
48. Morrow, C. A., Lockner, D. A., Moore, D. E. & Hickman, S. Deep permeability of the San Andreas Fault from San Andreas Fault Observatory at Depth (SAFOD) core samples. *J. Struct. Geol.* **64**, 99–114 (2014).
49. Lockner, D. A. & Byerlee, J. D. An earthquake instability model based on faults containing high fluid pressure compartments. *Pure Appl. Geophys.* **145**, 717–746 (1995).
50. Waldhauser, F. & Schaff, D. P. Large-scale relocation of two decades of Northern California seismicity using cross-correlation and double-difference methods. *J. Geophys. Res.* **113**, B08311 (2008).
51. Johanson, I. A., Fielding, E. J., Rolandone, F. & Burgmann, R. Coseismic and postseismic slip of the 2004 Parkfield earthquake from space-geodetic data. *Bull. Seismol. Soc. Am.* **96**, S269–S282 (2006).

Acknowledgements

This study was funded by National Science Foundation grants EAR-1357079 and EAR-1735630, and NASA Earth and Space Fellowship No. 80NSSC17K0371. The InSAR time series was obtained from refs [20,25]. The seismic catalogue was obtained from ref. [50]. The creepmeter data at Slacks Canyon were obtained from the United States Geological Survey. We greatly thank H. Perfettini and D. Shelly for comments and suggestions.

Author contributions

M.K. performed the data analyses and modelling, interpreted the results, prepared figures displaying the results and wrote the manuscript. M.S. contributed to modelling, interpretation and editing the manuscript.

Competing interests

The authors declare no competing interests.

Additional information

Supplementary information is available for this paper at https://doi.org/10.1038/s41561-018-0160-2.

Reprints and permissions information is available at www.nature.com/reprints.

Correspondence and requests for materials should be addressed to M.K.

Publisher's note: Springer Nature remains neutral with regard to jurisdictional claims in published maps and institutional affiliations.

Methods

Rate-and-state friction model. The effective normal stress $\sigma_e = \sigma_n - p$, where σ_n is tectonic normal stress and p is the pore pressure, is related to steady-state shear stress (τ_{ss}) through $\tau_{ss} = \sigma_e\left(f_0 + (\mathrm{a} - \mathrm{b})\log\frac{V_{ss}}{V_0}\right)$. In this equation, f_0 is nominal coefficient of friction, $a-b$ is the frictional rate parameter, V_{ss} is the steady-state rate and V_0 is the reference creep rate[41]. The shear stress change on the fault patch i between time steps t_1 and $t_2 = t_1 + dt$ is estimated[52] through $\tau(i, dt) = \overset{\mathrm{ij}}{\tau_0} dt + d\tau(i, dt)$, in which the first term on the right side is the stress due to tectonic plate loading[53] with $\overset{\mathrm{ij}}{\tau_0} = 0.25\,\mathrm{bar\,yr^{-1}}$. The second term accounts for the imparted stress due to slip on the adjacent fault patches, provided by $d\tau(i, dt) = \sum_{j=1}^{n} G(i,j)\,s(j, dt)$, where slip ($s$) on the fault, discretized into n dislocation patches, is obtained from the time-dependent model of creep along the CSAF from ref. [20]. The elastic kernel $G(i,j)$ represents the shear stress change at the patch i due to a unit rake-directed slip on patch j. This kernel is defined by the analytical solution of a rectangular dislocation buried in an elastic half-space[54], with Poisson ratio and shear modulus of 0.25 and 30 GPa, respectively. Supplementary Fig. 3b,c shows the temporal average and standard deviation of the shear stress rate on the CSAF. Without loss of generality, we choose $V_0 = V_{lt}(i)$ where $V_{lt}(i)$ is the long-term creep rate estimated for each fault patch along CSAF[20]. Time series of V_{ss}, which is considered as the rate of creep between consecutive time steps, is also obtained from the time-dependent model of creep from ref. [20]. Moreover, based on the laboratory experiments on SAFOD samples[5], frictional parameter ($a-b$) and coefficient of friction (f_0) are chosen to be 0.01 and 0.1 for the entire fault, respectively. Given that $\tau(i,dt)$ and, therefore, estimated σ_e are a function of interval between consecutive time steps, our estimates could be affected by irregular temporal sampling of creep model. Therefore, temporally normalized effective normal stress with respect to the period between consecutive time steps is presented and discussed throughout the paper. Spatial distribution of average rate of σ_e and its standard deviations are depicted in Supplementary Fig. 4.

Fault creep self-affinity analysis. A self-affine two-dimensional profile in the xy plane has constant statistical properties under an affine transformation of the form $\delta x \to \lambda \delta x$, $\delta y \to \lambda^H \delta y$, where λ is the scale factor and H is the Hurst exponent[29]. To investigate the self-affinity of a given profile, the method of Fourier analysis is widely used[55]. Through this method, Fourier power spectrum (P) as a function of wave number (k) follows a linear trend in log–log space, which is related to the Hurst exponent through $P(k) = Ck^{-1-2H}$, where C is the pre-factor. Thus, fitting a line to the log–log plot of $P(k)$ versus wave number k using a robust regression method enables the Hurst exponent and pre-factor as well as their standard deviations to be estimated. The Hurst exponent, ranging between 0 and 1, describes how the profile roughness changes with scale, with a smoother and more persistent trend in larger scales, for higher values. The pre-factor, C, gives information about the amplitude of roughness and is used for comparing the relative roughness of multiple profiles[56]. The black curve in Fig. 3b shows the temporal evolution of pre-factor estimated for the time series of fault-parallel profiles of the creep rate difference.

Gutenberg–Richter *b*-value. The Gutenberg–Richter law relates the frequency of occurrence to the magnitude of earthquakes through $\log_{10} N = a - bM$, where N is the cumulative number of events larger than magnitude M, and a and b are constants[57]. To obtain the parameter b (so-called b-value), we implemented the maximum likelihood estimation (MLE) method[58,59]. Using this method, $b_{\mathrm{MLE}} = \log_{10}(e)/[M_m - (M_c - \delta M/2)]$, where M_m is the mean magnitude, M_c is the magnitude of completeness, e is the Euler's number and the magnitudes are rounded to $\delta M = 0.01$. The associated standard deviation can also be calculated[60] using $\sigma_b = 2.30 \times (b_{\mathrm{MLE}})^2 \sqrt{\sum_{i=1}^{n} (M_i - M_m)^2 / n(n-1)}$, where n is the size of observation window, containing n earthquakes with magnitudes M_i. To avoid underestimation of the b-value, one needs to carefully consider the completeness magnitude (M_c) for a given seismic catalogue[61]. Following previous estimations of completeness magnitude for the seismic catalogue near the CSAF and Parkfield segment[43,62,63], we used $M_c = 1.3$. To account for the distribution of events near the fault surface, we assigned a distance-dependent weight to all the earthquakes in the vicinity of the fault[62]. We used an exponential weighting function[62], $w(D) = \zeta e^{-\zeta D}$, in which D is the closest distance between earthquake hypocentre and the fault surface, and $\zeta = 0.7$ after ref. [62]. We have tested various values of ζ ranging from 0.3 to 1.0 and all yield comparable results. Given its relatively homogeneous and fast rate of creep, we consider the central zone (20 to 90 km) for b-value calculation. The magnitude distribution of all the earthquakes considered for this analysis is shown in Supplementary Fig. 5.

Sorting the earthquakes based on the occurrence time, we used n number of events as the size of the moving window, without any overlap between consecutive windows, and estimated the time-dependent b-value[43]. The optimum size of this moving window is estimated through a Monte Carlo search algorithm[62]. To this end, we simulated 1,000 synthetic earthquake catalogues with true b-value of $b_0 = 1$, using $M = (M_c - \delta M/2) - \log(r)/\beta$, in which $\beta = \log(10) b_0$, and r is a set of random numbers between 0 and 1, produced using Matlab's 'rand' function[62]. The number of events in each synthetic catalogue and their weight as a function of distance from the fault are the same as that of the CSAF observed seismic catalogue. To identify the acceptable range of window size, we test a range of n from 50 to 300 with steps of 2. As a result, we obtain a time series of b-value as a function of n, per synthetic catalogue. Next, for each window size n, considering the estimated values for different time steps across all 1,000 simulations, we calculate the time series of mean b-value and associated standard deviation. For each window size, the highest standard deviation and the maximum difference between mean b-value time series and the true value of $b_0 = 1$ are considered as the representative precision and accuracy of the time series (Supplementary Fig. 6). The criterion for acceptable window sizes is the associated accuracy and precision being less than 5% and 10% of the true b-value, respectively. We find that the accuracy of the estimated mean b-value time series is acceptable for the window sizes of larger than ~60 events (Supplementary Fig. 6). However, considering the precision criterion, our Monte Carlo search algorithm results in an optimum window size of larger than 160 events (Supplementary Fig. 6). Our preferred b-value time series (Fig. 3) is estimated using a window size of 170 events, which yields a sampling rate of roughly half a year (Supplementary Fig. 7).

Coulomb failure stress. Time series of Coulomb failure stress change ΔCFS is estimated using the time-dependent model of creep on the CSAF from ref. [20]. The total shear ($\Delta\tau$) and normal stress ($\Delta\sigma$) imposed at the earthquake hypocentre in each time step is estimated as superposition of the stress imparted by creep at all patches across the CSAF[54]. The Coulomb failure stress change $\Delta \mathrm{CFS} = \Delta\tau - \mu\Delta\sigma$ is then estimated assuming a friction coefficient of $\mu = 0.6$ on a fault with the mean strike (313°) and dip (86°) of the CSAF.

Code availability. Computer code that supports the findings of this study is available from the corresponding author upon request.

Data availability. The InSAR time series was obtained from refs [20,25]. The seismic catalogue was obtained from ref. [50]. The creepmeter data at Slacks Canyon were obtained from the United States Geological Survey. The data and observational results that support the findings of this study are available from the corresponding author upon request.

References

52. Perfettini, H. & Avouac, J. P. Modeling afterslip and aftershocks following the 1992 Landers earthquake. *J. Geophys. Res.* **112**, B07409 (2007).
53. Parsons, T. Post-1906 stress recovery of the San Andreas fault system calculated from three-dimensional finite element analysis. *J. Geophys. Res.* https://doi.org/10.1029/2001JB001051 (2002).
54. Okada, Y. Internal deformation due to shear and tensile faults in a half-space. *Bull. Seism. Soc. Am.* **82**, 1018–1040 (1992).
55. Schmittbuhl, J., Vilotte, J. P. & Roux, S. Reliability of self-affine measurements. *Phys. Rev. E* **51**, 131–147 (1995).
56. Candela, T. et al. Roughness of fault surfaces over nine decades of length scales. *J. Geophys. Res.* **117**, B08409 (2012).
57. Richter, C. F. *Elementary Seismology* 768 (Freeman, San Francisco, 1958).
58. Utsu, T. A method for determining the value of b in a formula $\log n = a - bM$ showing the magnitude–frequency relation for earthquakes. *Geophys. Bull. Hokkaido Univ.* **13**, 99–103 (1965).
59. Bender, B. Maximum likelihood estimation of b values for magnitude grouped data. *Bull. Seismol. Soc. Am.* **73**, 831–851 (1983).
60. Shi, Y. & Bolt, B. A. The standard error of the magnitude–frequency b value. *Bull. Seismol. Soc. Am.* **72**, 1677–1687 (1982).
61. Woessner, J. & Wiemer, S. Assessing the quality of earthquake catalogues: estimating the magnitude of completeness and its uncertainty. *Bull. Seism. Soc. Am.* **95**, 684–698 (2005).
62. Tormann, T., Wiemer, S. & Mignan, A. Systematic survey of high-resolution b value imaging along Californian faults: inference on asperities. *J. Geophys. Res. Solid Earth* **119**, 2029–2054 (2014).
63. Schorlemmer, D., Wiemer, S. & Wyss, M. Earthquake statistics at Parkfield: 1. Stationarity of b values. *J. Geophys. Res.* **109**, B12307 (2004).